Reflection of surface waves by fault structures in granular media

MSc thesis: Raf Martens

student number: 6272177

Supervisors: Jasper Smits, Ernst Willingshofer

Abstract

Laser vibrometry has previously been studied as a new non-invasive imaging method to acoustically image physical analogue models. This study aims to characterize the interaction between acoustic waves and deformation zones in granular media to study the viability of using laser vibrometry as an imaging method. Physical and numerical models are used to study the effect of deformation zone properties and geometry on the wave behaviour. The results from these experiments show that there is no observable interaction with the body wave. The surface waves do show significant interaction with deformation zones. The properties and geometry of the deformation zone affect the reflection coefficient of surface waves. With an increase in thickness of the deformation zone, and an increase in density contrast between the deformation zone and the surrounding material, the reflection coefficient increases. The geometry of the deformation zone affects the waves mainly based on the dip direction. If the deformation zone dips away from the source, the surface wave has a very low reflection rate and passes through the zone with little reflection. When the deformation zone dips towards the source the refraction rate is high, little of the wave passes through the deformation zone and it partially reflects back. Thus, while the laser vibrometry method could be used to study the properties and geometry of faults at the surface, improvements are needed to be able to use it for imaging the internal structure of a granular material.

Table of Contents

1. Introduction

Some geological processes, like large scale deformation and the resulting fault structures, are too complex to be analytically understood. They can be hundreds of kilometers in size, and form on a timescale of millions of years, which makes them unfit for direct empirical experiments. Thus, to gain qualitative and quantitative insight into the evolution of such geological processes, physical analogue models are often used (Hubbert, 1937, Koyi, 1997). When modelling deformation in the brittle regime of the upper crust, analogue models are commonly made with granular materials. When deforming these materials the strain is accommodated in shear zones which function as an analogue to natural faults (Mandl, 1977).

Traditionally, information on the evolution of the internal structure in scale-models, like these shear zones, is retrieved in two ways. After ending the experiment multiple 2D cross sections of the model are made to study the final 3D structure and by studying the topography change of the model over time using digital image correlation techniques and extrapolating to interpret the internal structure. In some cases this second method is extended by including see-through walls as boundaries in the experiment to also study the outside 2D cross section over time (Adam 2005). This method is however very susceptible to boundary effects. Therefore neither of these two methods can directly study the evolution of the internal 3D structure of the faults inside the model.

Previously, a non-invasive methods that has been used to get around this lack of internal imaging is X-ray tomography (Colletta et al., 1991, Panien et al., 2006, Schmid et al., 2022, Zwaan et al., 2018 & 2023). This method can image the 3D structure based on multiple 2d-cross sections of the model during its evolution. However, X-ray scanning has some problems, it is rather elaborate and expensive technique which restricts the size of the model (Buddensiek, 2009). The size restrictions are caused by the size of the scannable area of the CT-scanner and by the ray absorption of the model, which if it gets too high can lead to data loss. Another problem with this method is the long cooldown time of a CT scanner, which leads to long timesteps between measurements.

Another imaging method that has been tested before is the use of acoustic waves. This method is similar to how actual geological structures have been imaged for decades. However, applying this method on this scale has proven difficult due to the attenuative properties of granular materials (Purnell, 1986; Sherlock, 1999). Shear zones are observed to undergo significant dilatancy, where the bulk density of the granular material decreases as a result of the flow of material (Pouliquen and Gutfraind, 1996, Wegner et al., 2014). Thus a density contrast is formed between the shear zone and the rest of the model. Because the velocity of acoustic waves is impacted by density differences it might be possible to image this density contrast, using acoustic methods.

Previously, piezoelectric transducers or low frequency shakers have been used to generate shockwaves (Krawczyk et al., 2013, Bodet et al., 2010 & 2014). However, this method of generating waves has the downside that the transducers and the shaker need to be buried within the material to be effective, and thereby restrict movement of the model. Additionally, for optimal results, the transducers require the experiment to be set in water-saturated sandbox models, for good coupling, which also limits practical use. While these methods still have some requirements that limit their usefulness in physical modelling, they could be used to image internal structure of an analogue model.

To overcome these issues a laser based vibrometry method as described by Smits et al. (In prep.) can be used. This method uses a laser beam, which is fired at the surface of the model, to create the acoustic waves. The use of a laser for both the source and the receiver means there is no physical connection between the measurement method and the model, meaning that this method does not

interfere with the evolution of the model, like the shakers would. It also has no size limitation on the model, like the CT scanner has. Thus, because it applies less restrictions on the model itself, the laser vibrometry method would be a more practical solution for studying physical analogue models. Using such a laser based system to acoustically image solid materials has been previously successful (Dewhurst et al. 1982, Chen et al. 2013), however, to use this method to acoustically characterize a granular material has only been attempted by Smits et al. (in prep.).

Generally, the acoustic based methods have not yet been proven to be able to acoustically image shear zones in the granular media of an analogue model. This has only been attempted by Buddensiek et al. (2009) who successfully studied reflections of acoustic waves on a deformation zone, created by pulling a wire through the model. Therefore, this study aims to further characterize the interaction between acoustic waves and deformation zones and shear zones in granular media, to predict the usefulness of this method in studying the 3D evolution of shear zones in analogue models.

1.1 Wave behaviour in granular materials

Mechanical waves can be broadly described as the propagation of a disturbance or displacement through a medium. In acoustics the vibrations of a material are studied to better understand the propagation of such waves.

When describing the different wave types in solid materials they are often referred to as: compressional waves (P-waves) and shear waves (S-waves). The P-waves propagate as compressions trough a medium as seen in Figure 1a. The S-waves propagate by means of shear stresses as seen in Figure 1b, this also means that this type of wave can only travel trough solids, as liquids and gasses don't support shear stresses.

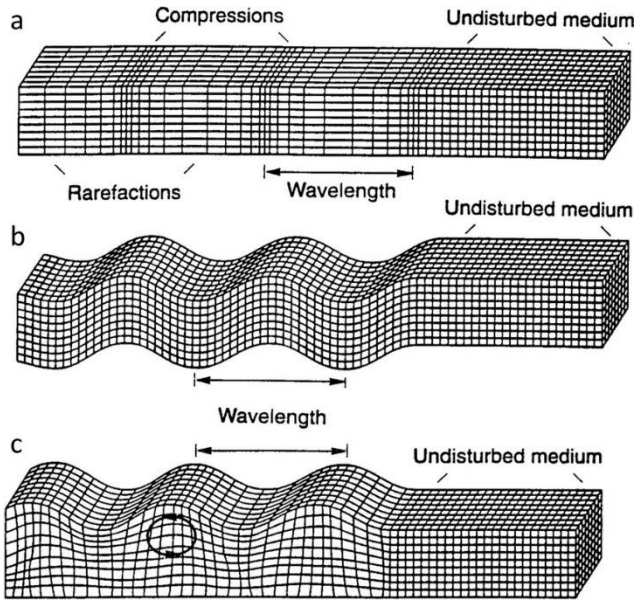

Figure 1: Displacement characteristics during propagation of the body waves: P wave (a) and S wave (b), and of the surface wave: Rayleigh wave (c) in an elastic solid. (Annotated figure from Nam et al., 2013).

The P-wave and S-wave are both body waves because they travel through the interior of the material. Then there is one other type of wave: surface waves. In elastic solids, these waves form by an interaction of the other two wave types at the free surface of a medium. They then propagate only along the surface of the medium as seen in Figure 1c.

Wave behaviour in granular material differs significantly of regular solid materials. The two body waves, the P-wave and S-wave still propagate in the same way, as seen in Figure 1a and b respectively. But, in the vicinity of the free surface of a granular medium the wave velocities of both the body waves are dependent on depth differently than in a solid (Gassmann, 1951).

The observed depth dependency of wave velocity can be explained using the dependency of the wave velocity on stress in the model. This can be expressed as a power law dependency on effective stress:

$$V_{P,S} = \gamma_{P,S}(\sigma'_v)^{\alpha_{P,S}}, \quad (1)$$

where $V_{P,S}$ is the wave velocity of either P- or S-waves, $\gamma_{P,S}$ is a depth-independent coefficient for P- or S-waves, mainly depending on the elastic properties of grains, porosity, and coordination number of the packed structure, $\alpha_{P,S}$ is the power-law exponent for either p- or s-waves and σ'_v is the effective stress (Bergamo and Socco, 2016). In the case of an unperturbed model, the effective stress can also be defined as lithostatic stress, where the stress is dependent on depth:

$$\sigma'_v = \rho g z \,, \tag{2}$$

where ρ is the bulk density of the material, g is the gravitational acceleration and z is the depth. Combining equation 1 with equation 2 this leads to an equation that can describe the depth dependency of the wave velocity:

$$V_{P,S} = \gamma_{P,S}(\rho g z)^{\alpha_{P,S}} \,. \tag{3}$$

This heterogeneity in granular materials also affects the behaviour of surface waves. In elastic solids the main surface wave type is the Rayleigh wave (Figure 1c), which forms as a combination of P-waves and S-waves. In granular media there are also waves propagating along the free surface composed of longitudinal P-waves and shear vertical (SV) waves. These P-SV waves are a type of Rayleigh wave, but in granular media these surface waves are not only a result of an interaction of the body waves with the free surface but also of the increasing rigidity of the granular material with depth (Gassmann, 1951, Aleshin, 2007). This increasing rigidity with depth causes an upwards bending of the waves which is known as the mirage effect (Liu & Nagel, 1992). These factors combined lead to a different type of surface wave, that does not behave like a typical Rayleigh wave. One of the features of this surface wave in a granular medium is that it appears in a multiple of modes (Jacobs et al., 2008, Tournat & Gusev, 2010, Zaccherini et al., 2021).

In previous experiments of acoustics in granular media, the different modes between the surface waves have also been observed. Two surface modes, with different speeds and wavelengths have been observed in acoustic experiments by Zaccherini et al. (2021), while Jacobs et al. (2008) has been able to distinguish 8 modes. The differing speeds between the modes can be attributed to the differing wavelengths of the surface waves. The lower modes have shorter wavelength and thus travel at a lower depth compared to the other modes, which means that, because of the depth dependency of the wave velocities, they travel through material with lower average wave velocities.

2. Methods

To better understand the effect of a deformation zone in a granular medium on acoustic waves, four parameter studies were done. In these four parameter studies two different modelling methods, physical and numerical, are used to study two types of parameters, deformation zone properties and geometry. These two different modelling methods are used together because combined they can provide a more complete understanding of the interaction between the acoustic waves and the deformation zone. The use of physical modelling will more accurately show the effects of the deformation zone on the waves, while the numerical modelling can be more precise. Comparing the results of these two methods will thus provide further insight on the interactions of acoustic waves and fault structures in granular media.

The effect of geometry can be studied in the same way using the two modelling methods. However, this is not the case for the effect of deformation zone properties. Two different deformation zone

properties are studied: thickness, in physical modelling, and density, in numerical modelling. These two properties were chosen because they could both influence the wave behaviour significantly. Both of them can however only be adequately studied with one of the used modelling methods. The density variation of the deformation zone is not studied in the physical model as there is no way to reliably implement the deformation zones with different bulk densities. The changed bulk density in physical analogue modelling is entirely dependent on the physical parameters of the material that is used. The thickness of the deformation zone is not studied using the numerical modelling because the variations in thickness needed to properly reflect the variations in the physical model require a much larger resolution than is currently used in the numerical model.

2.1 Physical modelling

In the physical modelling, laser vibrometry is used to measure the acoustic waves. The deformation zone property studied with physical modelling is the thickness of the deformation zone. This experiment is called PP. The effect of the geometry is studied by varying the dip angle and dip direction of the deformation zone in relation to the source receiver pair. This experiment is called PG.

2.1.1 Laser vibrometry

In the physical modelling experiments, laser vibrometry (Figure 2) will be used to acoustically image the model. With this method the acoustic waves are created by a laser that is aimed at the surface of the model. When activated, this laser hits a small area of the surface for a short amount of time. The grains that are hit with the laser then quickly heat up and thereby expand. After expanding they cool down and shrink again. This expansion and subsequent shrinking will generate waves from the point of impact of the laser. This point is thus the source of the wave. This conversion of heat energy to acoustic waves is known as the thermoacoustic effect. To then measure the created waves, a receiver is needed. Here a laser doppler vibrometer(LDV) is used which will record the vertical velocity of the particles at a specific spot of the surface of the model. Thus the wave will be created and measured using two laser based systems, requiring no physical connection to the model.

Both lasers are aimed at the model using a mirror set-up as seen in Figure 2. Figure 2a shows an image of the real life set-up in the lab, with both lasers situated behind the measured model. The laser used for the sources is a Qsmart 450 with a guide laser and beam attenuation module and a wavelength of 1064 nm. It is used at a pulse energy of 40 mJ. The LDV is aimed at a different location of the sample using a similar mirror set-up. The model LDV used is a Vibroflex QTec from Polytec with the high pass filter set to 250 Hz and a bandwidth of 50 kHz. This set-up allows us to change the location of the source by changing the position of the final mirror using a rotational stepper motor. Changing the source location is easier in this set-up because the LDV laser needs to always be aimed at the sample with an angle of 90 degrees to the surface and the source laser does not. If the angle of the LDV laser to the surface changes it would no longer measure the pure vertical velocity but also partly a horizontal component, the amount of which changes depending on the angle. Thus keeping the angle of the LDV laser and the surface constant is important. Changing the position of the source between measurements means the used set-up has a single fixed receiver point compared to a variable source point.

An example of a trace from a single measurement of one source receiver pair can be seen in Figure 3a, where time is on the x-axis and the measured velocities on the y-axis. To obtain a dataset of high enough resolution around the deformation zone, the source points will be shot in a line of 15 centimeters as seen in Figure 2 with half a centimeter between the source points. This line starts one centimeter away from the receiver. For every source point a total of 20 twenty of these measurements are made. These 20 measurements are then averaged, filtered using a bandpass filter and gained to reduce the signal to noise ratio significantly resulting in the trace seen in Figure 3b.

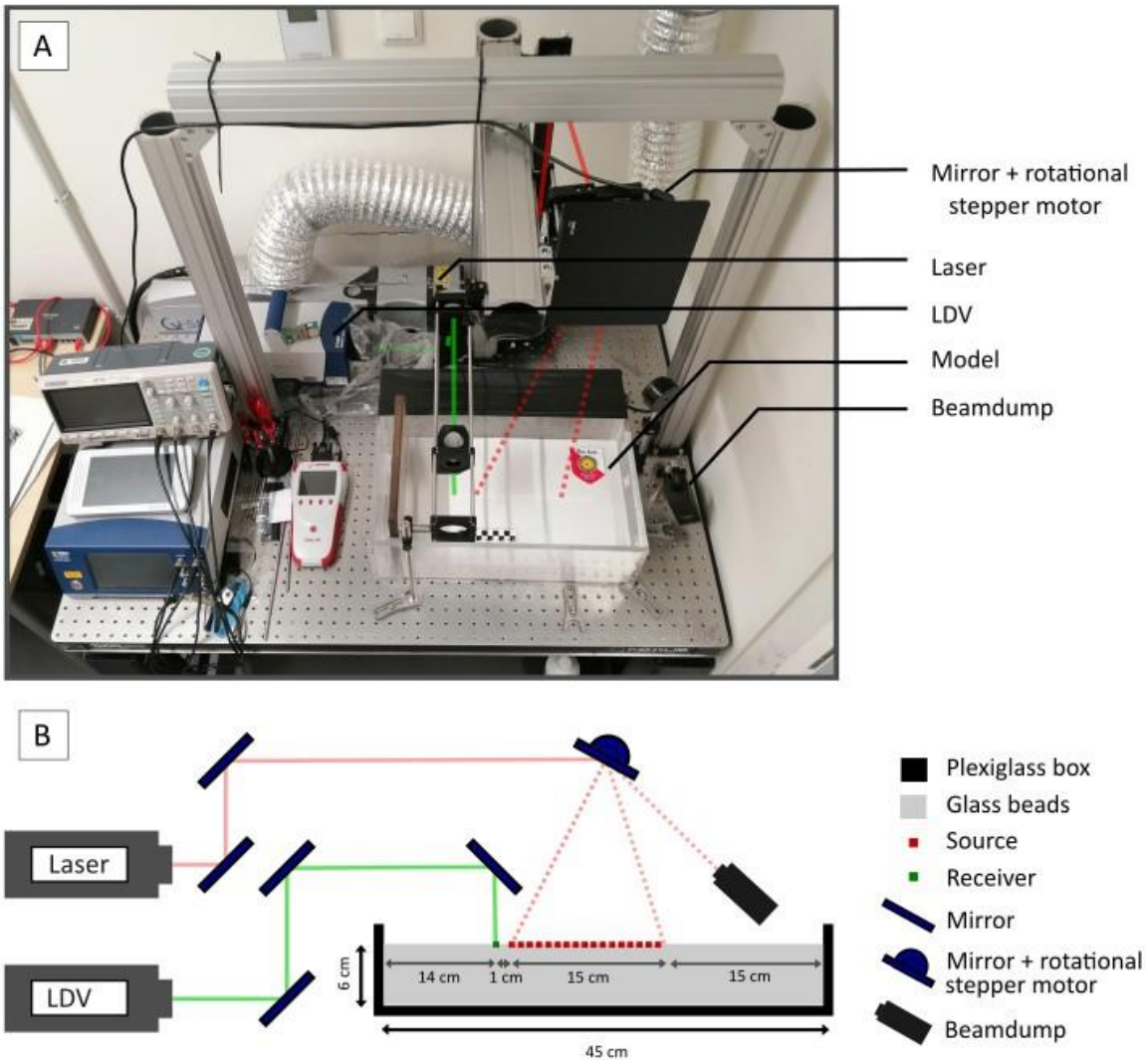

Figure 2: Overview of the physical modelling measurement set-up. With a picture of the vibrometry set-up in the lab (A),where the paths of the lasers beams are indicated in green and red. And a schematic view of the laser vibrometry system (B), including the Laser and the laser doppler vibrometer(LDV). Both lasers are redirected to the hit the model surface vertically using a mirror set-up. The mirror + rotational stepper motor allow the laser to be aimed at different location in th e model or at the beamdump.

These filtered traces for each of the source points are then plotted together corresponding to the location of the source in the line as seen in Figure 3c. This new plot is known as a wiggle plot, which has time on the y axis compared to the earlier plots. In these types of plots the velocity of the wave types in the granular medium can be determined. To produce the final acoustic profile the individual traces are then not plotted as lines but as a density plot, which can be seen in Figure 3d, to increase readability of the wiggle plot. This is the final acoustic profile used to compare the results of the experiments.

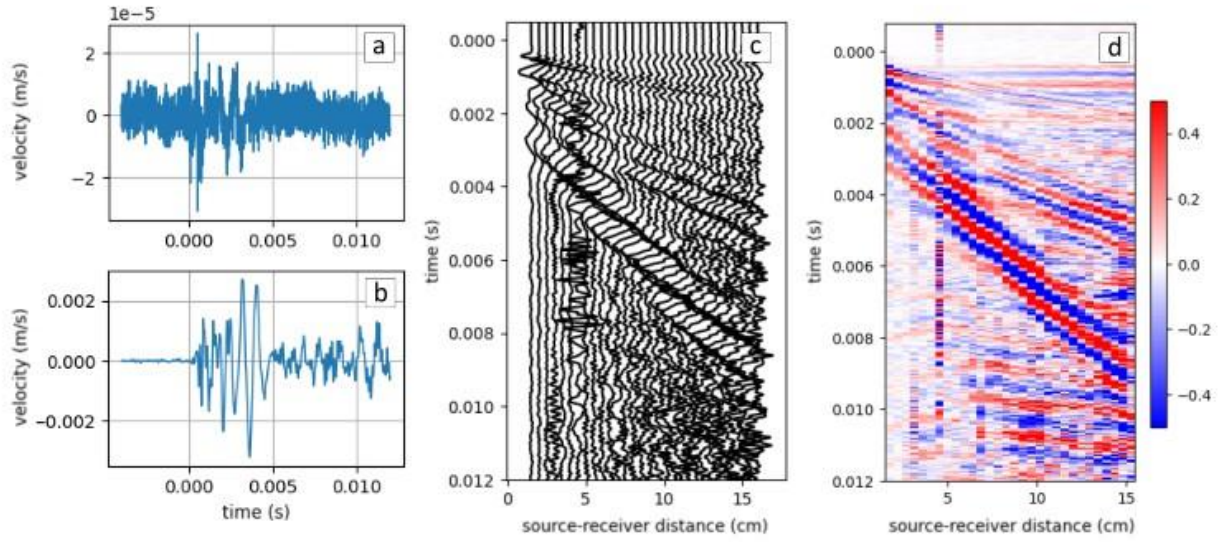

Figure 3: Data processing steps from raw data to wavefield density plots. (a) The raw velocity data acquisition after background subtraction and stacking for a single measurement, (b) the filtered, gained and averaged velocity data for a single source receiver pair, (c) A wiggle plot with measurements of all source receiver pairs and (d) the final wavefield density plot.

2.1.2 Physical model set-up

For the physical modelling a plexiglass box with dimensions 45 x 25 x 15 cm is used as seen in Figure 4. Glass beads serve as the granular medium because they are both well sorted and perfect spheres. These properties have been previously observed to provide the best signal to noise ratio, and the least amount attenuation (Appendix I, Krawczyk et al. 2013). The glass beads have a diameter of 100 µm to 200 µm and a bulk density of 1530 kg/m^3 (Klinkmüller et al. 2016). The frictional properties of glass beads of this size have also been determined by Klinkmüller et al. (2016) and can be found in table 3 of this work with material name GFZGLB 100–200 µm. The beads are sieved into the box by hand using sieves with a mesh size of 300 µm. During sieving the sieves are kept at a regular height of about twenty centimeters above the model to keep the distribution and density of the glass beads as consistent as possible. A layer of glass beads is sieved to a thickness of six centimeters similar to the experiments of buddensiek et al., (2009).

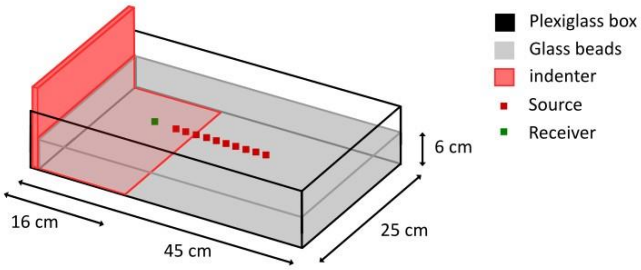

Figure 4: 3D Schematic view of physical model set-up.

After the samples are sieved either a deformation zone or fault is created in the model. These structures are created with two different methods. Both method use a L-shaped indenter as can be seen in red in Figure 4. This indenter is put within the box before sieving. To create a fault zone, the indenter is then pushed incrementally by hand to create horizontal shortening within the model. First up to 6 mm to build up stresses, then up to a total of 12 mm until a thrust faults forms naturally off of the tip of the L-shaped indenter as seen in Figure 5 a. To create a deformation zone a wire is placed at the bottom of the box, which is also buried during sieving. The L-shaped indenter is still pushed into the model to apply shortening and build up stresses, but only 0.6 cm as to not create a fault yet. This is done to generate a similar stress field as in the other experiments. This also has the benefit that the increased stress decreases attenuation (Tournat and Gusev, 2010). The deformation

zone is then created by pulling the wire from the bottom through and out of the experiment (see Figure 5b). This method has the benefit that it allows for greater control on the location, angle and thickness of the deformation zone.

To single out the effect of the deformation zone on the acoustic profile, multiple acoustic profiles are acquired per model corresponding to the three steps in Figure 5. The first acoustic profile is acquired after sieving of the model (step 1), it allows for determining the specific acoustic profile after the sieving the model. The second measurement is acquired after the initial shortening of 0.6 cm (step 2), this will show the added effect of the shortening for each model. Then thirdly the final acoustic profile is acquired after the deformation zone or fault zone has been formed (step 3), comparing this result with the second measurement will show the exact effect of the deformation zone or fault zone on the acoustic profile.

Finally, for certain experiments the CT scanner is used to image the lower density zones in some of the experiments. The lower density zone will have a lower absorption coefficient for X-rays used in the CT scan and thus show up as a distinguishable zone on a CT scan. This allows us to create high resolution images of the internal structure to compare whether the expected fault structure is formed and to measure the structure of the deformation zones.

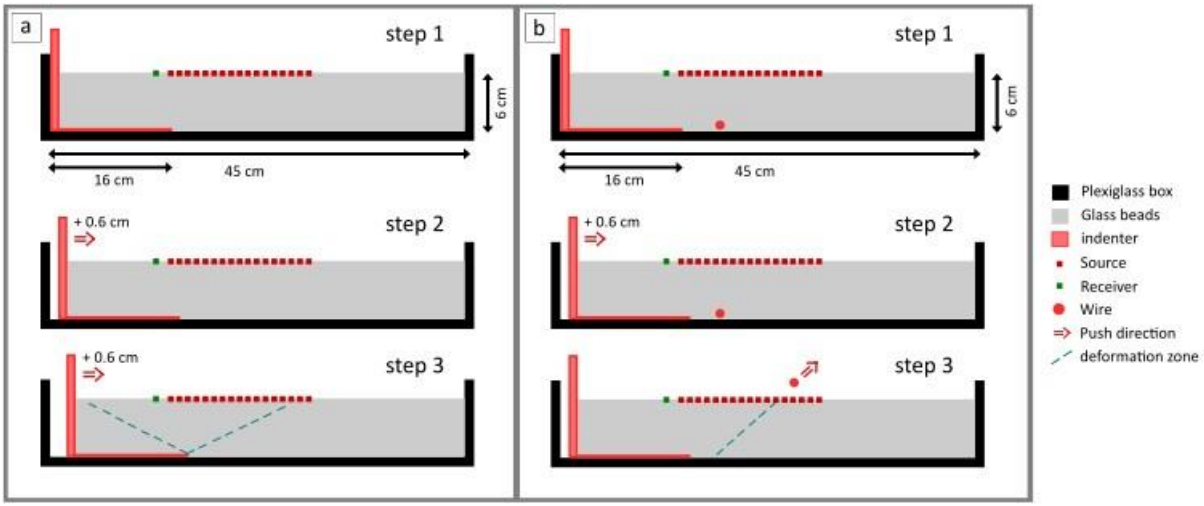

Figure 5: schematic cross section of the physical model showing the three steps for deformation of the model to create: a fault zone (a) or a deformation zone (b). Step 1 shows the model after the model has been sieved, and no deformation has occurred yet. Step 2 shows the model after the initial 0.6 cm shortening has been applied. Step 3 shows the model after a fault zone has formed due to the increased shortening (a) or the deformation zone has formed due to the removal of the wire (b).

2.1.3 Deformation zone properties PP

Four physical experiments are done to test the effect of the thickness of deformation zone, named PP.1, PP.2, PP.3 and PP.4. The first experiment(PP.1)contains a thrust fault made by shortening of the model as can be seen in Figure 5a. The other three experiments(PP.2, PP.3 and PP.4) contain deformation zones created using the wire method as can be seen in Figure 5b. To create deformation zones with different thicknesses three different wires are used. These different wire types are:

fishwire (PP.2), metalwire (PP.3) and rope (PP.4). These three wire types have diameters of 0.5mm, 1mm and 3 mm respectively. The wires will be pulled through the model at an angle of 45 degrees, exiting the model 10 cm away from the receiver. Because the thrust fault formed on the outer edge of the measurements, the acoustic profile will be extended with five centimeters (ten source points) in this experiment, to properly include the fault zone. The CT scanner will be used to look at cross sections of these models, so the thicknesses of the deformation zones and the thrust faults can be measured.

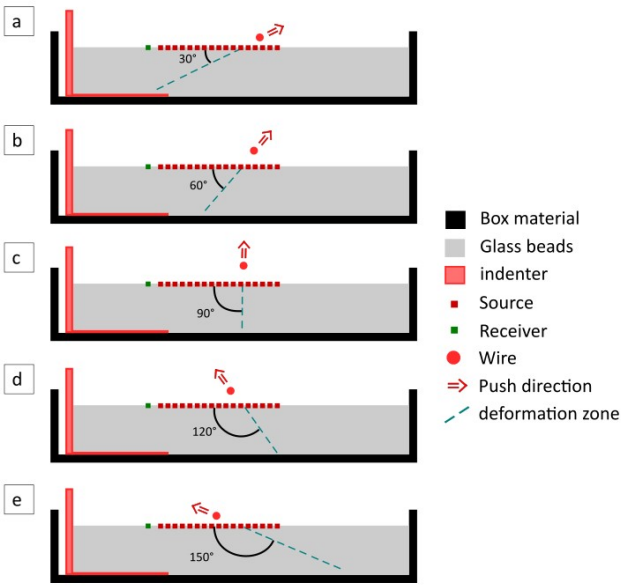

Figure 6: schematic view of cross sections of the different deformation zones of models PG.1 (a), PG.2 (b), PG.3 (c), PG.4 (d), PG.5 (e).

2.1.4 Deformation zone geometry PG

To test the effect of the geometry of the faultzone on the surface waves, five experiments are done containing deformation zones with differing dip angles and dip direction. The rope, with a diameter of 3 mm, is used to create the deformation zone at the appropriate angles. The dip-angles used are towards the receiver: 30, 60, 90, 120 and 150 degrees, for experiments PG.1, PG.2, PG.3, PG.4 and PG.5 respectively, an illustration is given in Figure 6. The outcrop of the fault at the surface is always located at the same distance of 11 centimeters from the receiver.

2.2 Numerical modelling

The numerical modelling method makes use of a waveform solver program. The property of the deformation zone studied with numerical modelling is the density contrast, in experiment NP. The effect of geometry is studied by varying the dip angle and dip direction of the deformation zone in relation to the source receiver pair, in experiment NG.

2.2.1 Numerical model set-up

For the waveform modelling the program Salvus (Afanasiev et al., 2019) software package is used to model expected acoustic profiles from the experimental setup. Within this program a set-up is made that corresponds to a vertical cross section of the physical model. One significant change is made to the model, the depth is increased from 6 centimeters to 26 centimeters. This change fully eliminates the reflection of the bottom of the box. The model itself is made up of mesh of about 600 points within the confines of the box used in the physical modelling, a rectangle with sides of 26 by 45 centimetres. At the edges of the box absorbing boundary conditions are used to simulate the reflections at a free surface.

The receivers and source are placed on the border of the box. In contrast to the physical model, the numerical model is set up with one source and multiple receivers. This significantly reduces the computing time needed and should give similar results. The source and receivers are placed at the top of the model as shown in Figure 7. The sources implemented at x = 15 m, followed by thirty receivers in a line from x = 16m to x = 31 m. For the creation of the wave a ricker wavelet is made at the source point according to a predetermined frequency. The wave formation is centred around time = 0.

This model requires an input of an s-wave velocity field (Vs) and P-wave velocity field(Vp), these fields need to be implemented slightly larger than the model itself to better allow for resolving of the waves. Using equation 3 these two velocity fields can be calculated based on the input of a bulk density, depth, gravity, and the constants: $\alpha_{P,S}$ and $\gamma_{P,S}$, the chosen values for these constants are seen in Table 1. These values for $\alpha_{P,S}$ and $\gamma_{P,S}$ give similar results to wave traveling through glass beads in the analogue models. They are also consistent with previously estimated values, which were determined measuring the GSAMs dispersion at a free surface (Jacob at al. 2008, Bodet et al. 2010, Bodet et al. 2014.).

To implement a deformation zone in the model a custom bulk density field will be used. The bulk density field can be used to simulate a deformation zone because in the bulk density is reduced in shear zones due to the process of decompaction. Thus an area of lower bulk density will approximate a deformation zone. The initial bulk density of the model is based on the bulk density of the glass beads used in the physical modelling of 1530 kg/m^3 (Klinkmüller et al. 2016). An example of a zone of lower bulk density be seen in Figure 8a. This bulk density field in combination with the other parameters then allows for the computation of the velocity fields in the model as can be seen in Figure 8b.

After running the model, the data from the receivers are gathered and the Y-component of the amplitude wave data is plotted directly in a wavefield density plot, to easily compare the numerical data to the physical data.

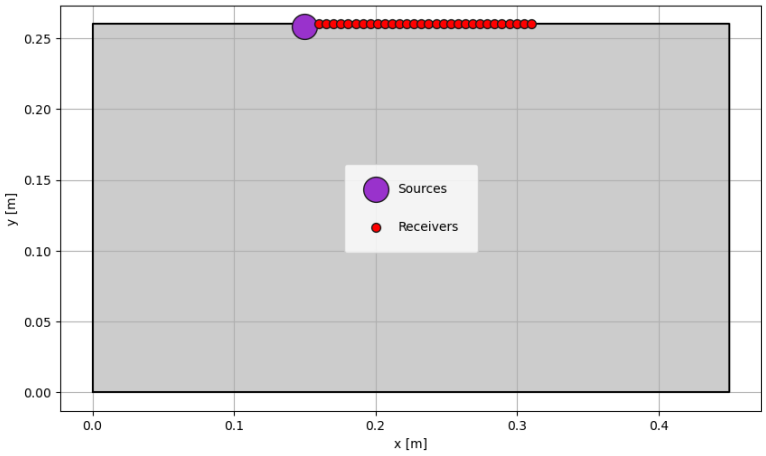

Figure 7: 2D boxdomain of the numerical model with the locations of the source and receivers indicated. The black rectangles indicates the size of the simulated box.

Bulk density (ρ) (kg/m^3)	1530
α_S	0.25
α_P	0.25
γ_S	8.2
γ_P	21.0
Wavelet freq. (Hz)	500
Max simulation freq. (Hz)	1100
End time (s)	0.008
Receiver amount	30

Table 1: Parameters used for the set-up of the numerical model.

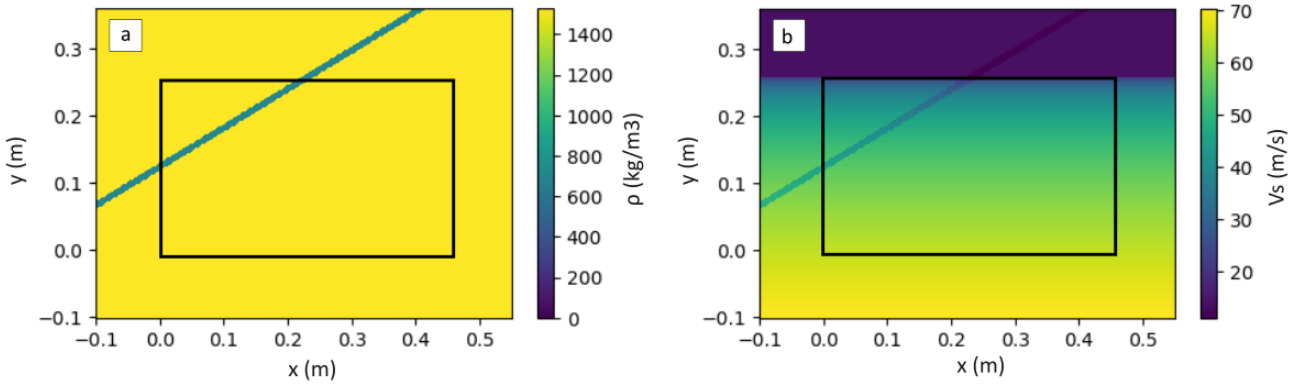

Figure 8: Plots of values of density field (a) and corresponding S-wave velocity field (b) showing the effect of the implementation of the lower density zone on the S-wave velocities. The black rectangles indicates the size of the simulated box.

2.2.2 Deformation zone properties NP

To study the influence of a deformation zone density a lower density zone of 1 cm thick will be implemented into the model at an angle of 45 degrees, dipping towards the source. The will intersect the surface of the model in the middle of the receivers at 8.5 centimeters away from the source. Four different models will be run. The first without a density anomaly (NP1), and three with lower density zones of: 1300 (NP2), 1000 (NP3) and 700 kg/m^3 (NP4). These coincide with a density decrease of 13%, 35% and 53%. The amount of packing density decrease in analogue models has been previously observed to be between 9 and 16% (Wegner et al., 2014).

2.2.3 Deformation zone geometry NG

To determine the influence of the angle difference of these density anomalies, multiple models will be run with lower density zones at different angles. These lower density zones will have a bulk density of 700 kg/m^3 and will always outcrop on the surface of the model in the middle of the receivers at 8,5 centimeters away from the source. The lower density zone will have dip angles of 30, 60, 90, 120 and 150 degrees towards the source, analogous to experiment 2.

3. Results

In this section the results of the four parameter studies will be discussed per modelling method. An overview of the general results for that modelling method will be discussed first, then the results per experiment. The results per experiment in the physical modelling are the thickness of the deformation zone (PP), then the dip angle and dip direction (PG), these are then followed by the two studies in the numerical modelling, density contrast of the deformation zone (NP), and finally dip angle and dip direction (NG).

3.1 Physical modelling results

For a complete overview of the results of the physical modelling it is necessary to both discuss the structural changes in the model and the acoustic profiles. Firstly an overview of the structural changes in the model will be given then the general acoustic data will be shown. As an example for both, the data of experiment PP1 will be used.

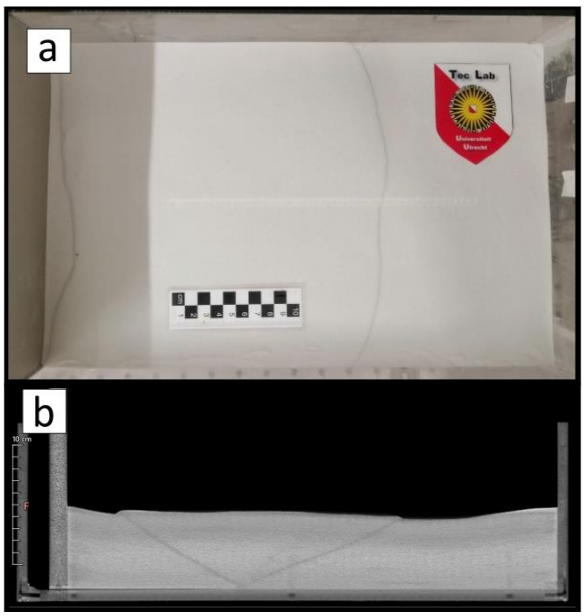

Figure 9: The final state of the model in experiment PP1 showing the formed structures. Top view of the model showing the created topography (a) and a CT scan cross section of the model showing the internal fault structure (b).

The final state of the model in experiment PP1 can be seen in Figure 9, with both a top view (Figure 9a) and a CT-scan image of a vertical cross section of the model (Figure 9b). Here some structural features can be identified at the surface of model and internally, these structures are created by both the measuring method and the applied deformation to the model. The laser used in the vibrometry method to create the source point has deformed the surface. Small craters are formed during the impact of the laser, creating some small scale topography of about a millimeter in height along the line of source points. Due to the recoloration of the glass beads after heating the area of these small craters are coloured whiter than the surroundings. The other visible topography structures are created by faulting and the implementation of deformation zones. In Figure 9b the two faults created by the indenter can be

seen with the resulting surface topography. Both originate from the bottom of the model at the furthest point of the bottom of the L-shaped indenter, as can be seen in the CT-scan image. The measured fault is located in the centre of the model. This fault also has visible boundary effects of the sides of the box in the fault structure. The fault plane is increasingly more curved closer to the edges of the model.

The acoustic profiles acquired using the physical modelling can be seen in Figure 10a-c. All profiles have distinguishable waves for at least part of the measured area due to a sufficiently high signal to noise ratio. This ratio does depend on the source-receiver distance, it is high for the shorter distances, but the further the distance between the source and the receiver, the lower the signal to noise ratio becomes. Thus in some experiments the waveform cannot be distinguished at longer source-receiver distances.

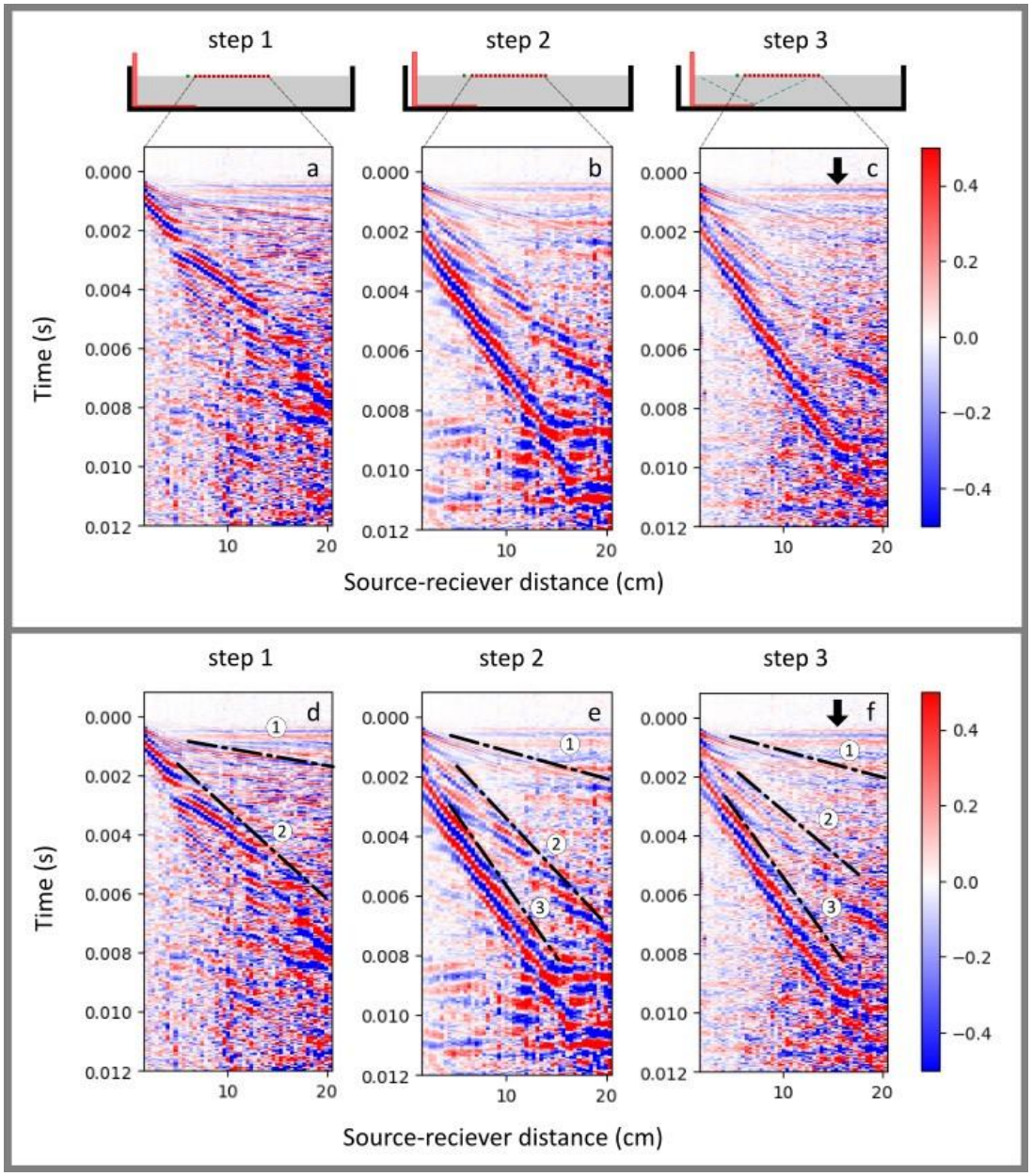

Figure 10: The three acoustic profiles per experiment. The acoustic profiles for experiment PT1 (a-c) and the acoustic profiles for experiment PT1 (d-f) with dashed lines indicating the first arrival of specific waves. The profile of step 1 is taken after sieving of the model, the profile of step 2 is taken after initial shortening of the model. The profile of step 3 is taken after the formation of a deformation zone. The black arrow indicates the location of the fault zone.

There are three wave types that can be distinguished in the acoustic profiles, these types are annotated in Figure 10d-f. After initially sieving the model two of these waves can be distinguished in the acoustic profile, numbered 1 and 2 according to their arrival time (see Figure 10d). For low source receiver distances these two waves are not yet distinguishable, because they overlap. After more than 3 to 4cm the single waveform has split into the different types with different characteristics. The first wave, wave 1, travels at around ~180 m/s and has a small wavelength. This wave can be considered the first arrival of a P-wave in the experiment. Wave 2 in Figure 10d has a longer wavelength and travels at a lower velocity of ~75 m/s. This is interpreted to be the arrival of a P-SV wave.

After the initial shortening multiple differences in the acoustic profile can already be observed, see Figure 10b, the amount of noise is decreased significantly throughout the model. Wave 1 travels slower at a velocity of ~150 m/s. The arrival of the second wave appears unaffected, but a third wave can now be distinguished (see Figure 10e). This wave is arrives later than the previous two waves and travels at a velocity of ~30 m/s. Wave 2 and 3 are both interpreted to be surface waves, named P-SV1 and P-SV2 corresponding to their arrival time. While these three wave types can be seen throughout all experiments, the wave velocities of the P-SV waves slightly differ between experiments. P-SV1 is interpreted to be the faster second mode of the surface waves, and P-SV1 is interpreted to be the slower first mode.

While the general behaviour of the signal to noise ratio, attenuation and waves stays consistent between experiments the absolute values of the signal to noise ratio and some wave parameters as well as the amount of attenuation in the model differ significantly between experiments. Thus in the results section an acoustic profile of the same experiment pre deformation but after shortening (step 2) is always included with the final measurement after deformation(step 3) to properly show which features in the acoustic profile are caused by the deformation zones and which are caused by other factors in the preparation of the model.

3.1.1 Deformation zone properties PP

The thicknesses of the differing deformation zones formed in this experiments are measured firstly using CT scanner data (see Table 2). The fish wire creates deformation zones of a similar thickness to thrust faults in this medium. The metal wire and rope create deformation zones with exaggerated thicknesses, the metal wire creates zones that are 1.5 times as thick as thrust faults, the rope creates zones that are 2 or more times as thick. When removing the wire from the model two elongated hills are formed with a topography of a few millimeters on both sides of where the wire exited the glass beads.

Figure 11shows the effect of the different thicknesses of the deformation zones on the acoustic waves. The P-wave is unaffected by the deformation zone in all four experiments. The P-SV waves show three effects caused by this zone. These effects are only distinguishable in the wire deformation zone experiments PP2, PP3 and PP4. Firstly both P-SV1 and P-SV2 show a reduced signal strength at the location of the fault zone for experiment PP2, PP3 and PP4 in Figure 11f, g and h respectively. Secondly in experiment PP3 an increase in wave speed of the P-SV2 to ~55 m/s can be observed after it has passed through the deformation zone. Thirdly, in experiment PP4 some reflection of the P-SV waves on the deformation zone can be observed. This reflected wave propagates in the opposite direction and has a significantly lower signal strength. It has a similar wavelength to both P-SV waves and a velocity of ~50 m/s, which is in between the velocities of P-SV1 (~75 m/s) and P-SV2 (~25 m/s). It is possible these reflection are also visible in PP3 (Figure 11g) but this is not clear enough.

MODEL NAME	DEFORMATION TYPE	WIRE THICKNESS (MM)	DEFORMATION ZONE THICKNESS (MM)
PP1	**FAULTING**	-	3-4
PP2	**FISHWIRE**	0,5	3
PP3	**METALWIRE**	1	4,5 – 5,0
PP4	**ROPE**	3	8

Table 2: Deformation zone thicknesses per deformation method as measured from CT scan imaging.

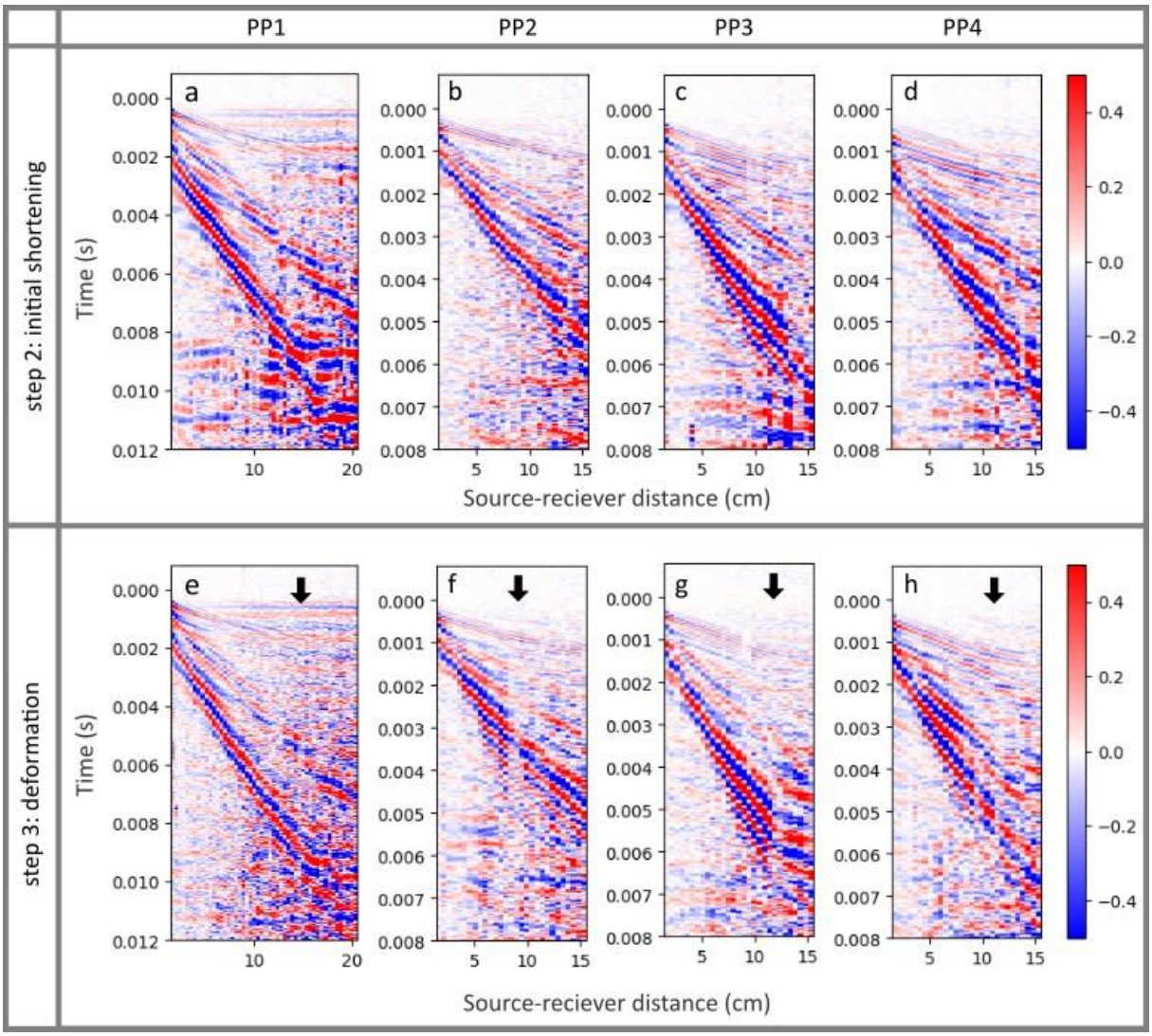

Figure 11: Acoustic profiles of deformation zone thickness experiments: (a, e) PP1, (b, f) PP2, (c, g) PP3 and (d, h) PP4. With (a-d) after step 2: initial shortening and (e-h) after step 3: deformation. The black arrow indicate the location of the deformation zones.

3.1.2 Deformation zone geometry PG

Figure 12 shows the effect of the difference in dip angle and dip direction of a deformation zone on acoustic waves. The P-waves show no effect of passing through the deformation zone in any experiment except for PA5, where a small hitch in the P-wave can be seen at the location of the deformation zone but no lasting change in the wave arrival times. The two P-SV waves are however affected by the deformation zone in all experiments. In experiment PG1 and PG2 a small increase in wave velocity of the PS-V2 wave can be observed after it has passed through the deformation zone. This effect is the most visible in experiment PG1 (Figure 12f). In experiment PG4 and PG5, where the deformation zone dips away from the receiver, the signal strength of both P-SV1 and P-SV2 are reduced after passing through the deformation zone. In experiment PG1, PG2 and PG3 some reflection of the P-SV waves on the deformation zone can be observed, as waves that are propagating in the opposite direction. This reflection is the most visible in PG1(see Figure 12f). No reflected waves can be observed in experiments PG4 and PG5.

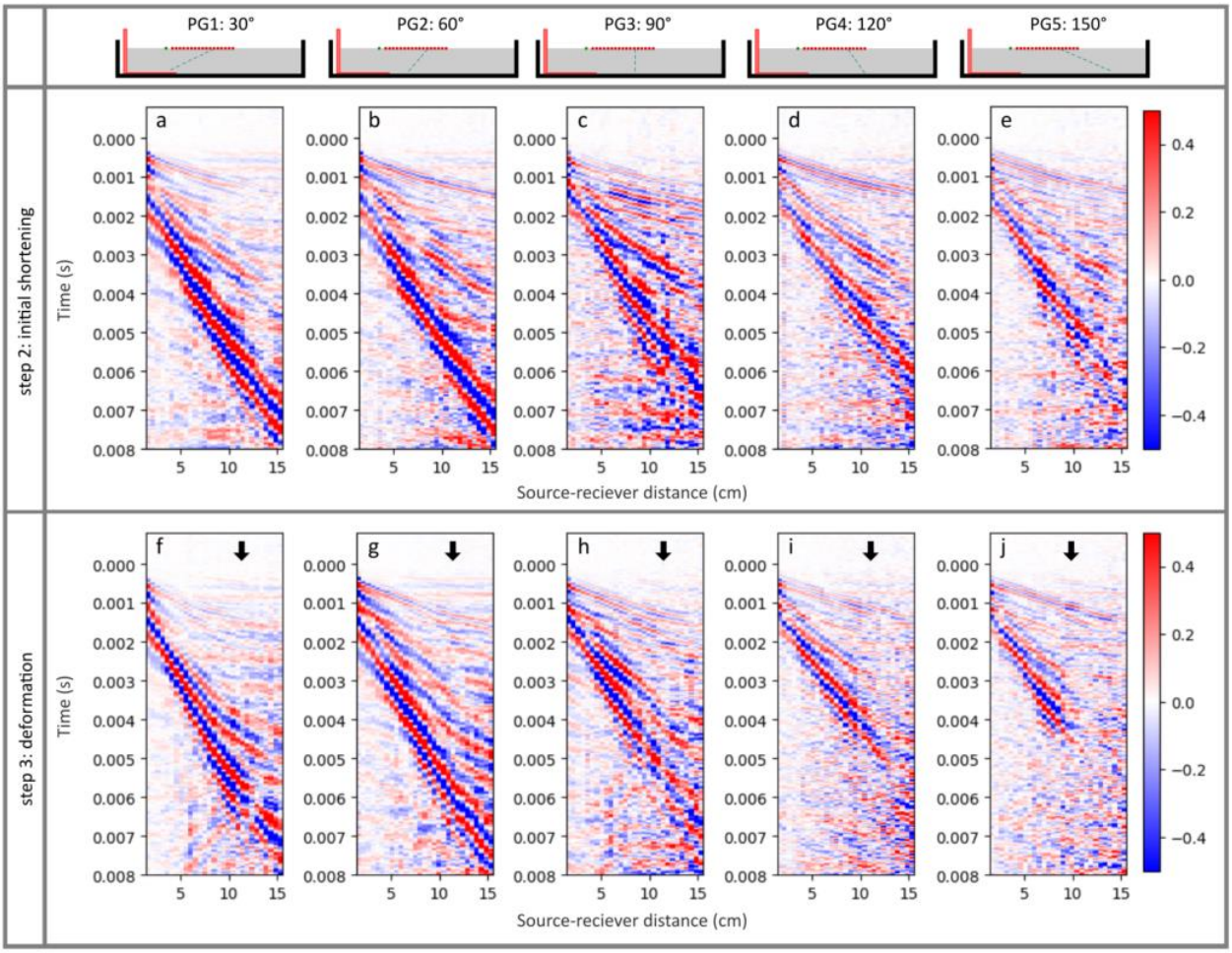

Figure 12: Acoustic profiles of deformation zone geometry difference experiments. PG1 (a,f), PG2 (b, g), PG3 (c, f), PG4 (d, j) and PG5 (e, j). The two acoustic profiles per experiment are from before and after deformation with step 2: initial shortening (a-e) and step 3: after formation of the deformation zone (f-j). The black arrow indicates the position of the deformation zone. A schematic cross section of the corresponding fault structure is imaged above the corresponding acoustic profiles.

3.2 Numerical modelling results

The numerical modelling method provides very consistent results, thus a singular model without a deformation zone can be used as a reference model for all following models. For this purpose the acoustic profile of experiment NP1 will be used. To properly validate the results from the numerical modelling a comparison with the physical results is needed. Figure 13 shows a comparison between the acoustic data of the numerical refence model and the acoustic data of a physical model. The physical modelling acoustic data used is from experiment PP1, without a deformation zone, but after initial shortening (step 2).

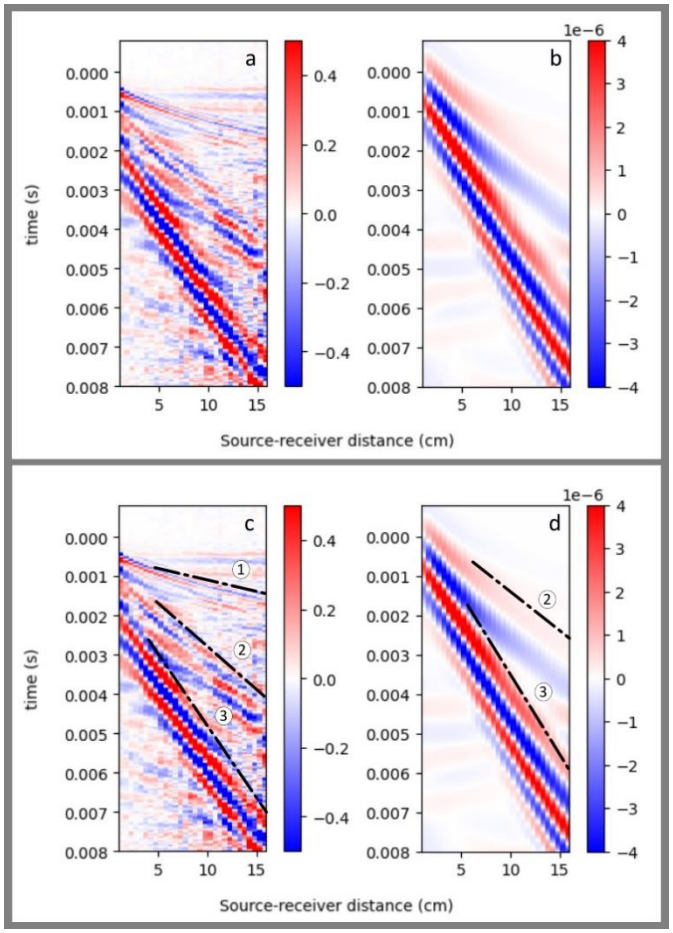

Figure 13: : comparison between numerical modelling and physical modelling without a deformation zone. The acoustic profile of physical modelling (a, c) is from experiment PP1 step 2 and the acoustic profile from numerical modelling (b, d) is from experiment NP1. The numbered dashed lines indicate the first arrival of a specific wave.

The signal to noise ratio in the numerical model is high, due to the low amount of noise, thus the different wave types are clearly distinguishable. After the wave has passed some horizontally orientated repeating features are still visible. There are two wave types that can be distinguished in the numerical model, they are annotated with the numbers 1 and 2 in Figure 13d corresponding to their arrival time. These two waves start of singular and split into the two distinguishable waves with different wave speeds after 6 cm (Figure 13). The wave numbered 1 is the fastest of these two wave types with a velocity of ~60 m/s. This wave has the longer wavelength of the two waves, and a significantly lower amplitude than the second wave. This wave can be interpreted as the P-wave that can also be seen in the physical model data. The slower wave has a smaller wavelength and a wave velocity of ~35 m/s. It is interpreted to be the P-SV wave of the physical data. No secondary P-SV wave is observed in the numerical modelling.

3.2.1 Deformation zone properties NP

Figure 14 shows the acoustic profiles of the deformation zone density contrast experiments. The P-wave does not change significantly when it passes through the low density zone, the amplitude of the wave is lowered slightly. The P-SV wave is also not affected by a low density contrast deformation zone, but in experiment NP3 and NP4 with high density contrasts, the wave experiences a delay when passing through the low density zone of about 0.5 milliseconds. Afterwards the wave travels slightly faster.

Reflections can be observed for all density contrasts. Two different reflected wave types can be distinguished based on their wave velocities, numbered 1 and 2 in Figure 14e based on their arrival time. In experiment NP2-4 wave 1 with a low amplitude and a velocity of about ~60 m/s can be observed propagating in the opposite direction. In experiment NP3 and NP4, Figure 14c and d respectively, the second reflected wave can be observed. This wave arrives later and has a velocity of about ~30 m/s. The amplitude of the reflected wave increases with increasing density contrasts.

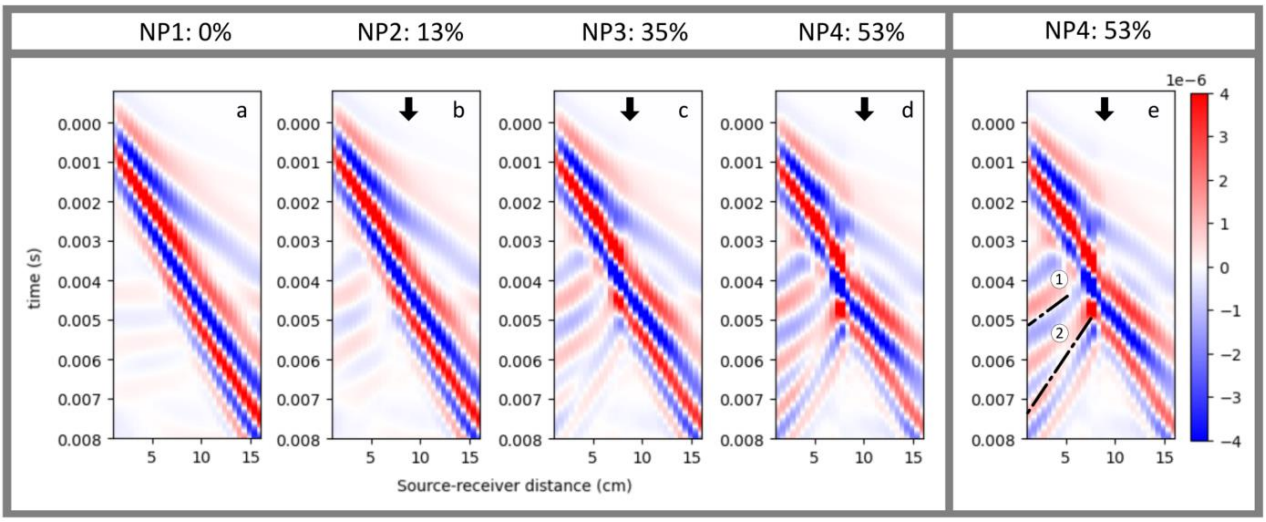

Figure 14: acoustic profiles of experiments NP1(a), NP2(b), NP3(c) and NP4 (d, e), with a low density zone density contrasts of 0%(a), 13%(b), 35%(c) and 53%(d, e). The numbered black dashed lines indicate the reflected wave types and the black arrows indicate the location of the low density zone.

3.2.2 Deformation zone geometry NG

The acoustic profiles of experiment NG1-5 in Figure 15 show a correlation between the acoustic waves and the angle of the low density zone. The P-SV1 wave does not change significantly when it passes through the low density zone, except for a slight reduction of amplitude. In models NG1, NG2 and NG3 a delay in the P-SV2 is observed when passing through the deformation zone of about 0.5 milliseconds.

In all five experiments some reflections can be seen. Again two different reflected wave types can be distinguished based on their wave velocities. The fastest of these two waves has a velocity of ~60m/s and can be observed in all experiments. It's amplitude decreases for increasing angles, in experiment NG5 it is only barely visible. The slowest of these two reflections has a velocity of ~30 m/s. It can only really be observed in experiment NG1, NG2 and NG3, not in the other two experiments.

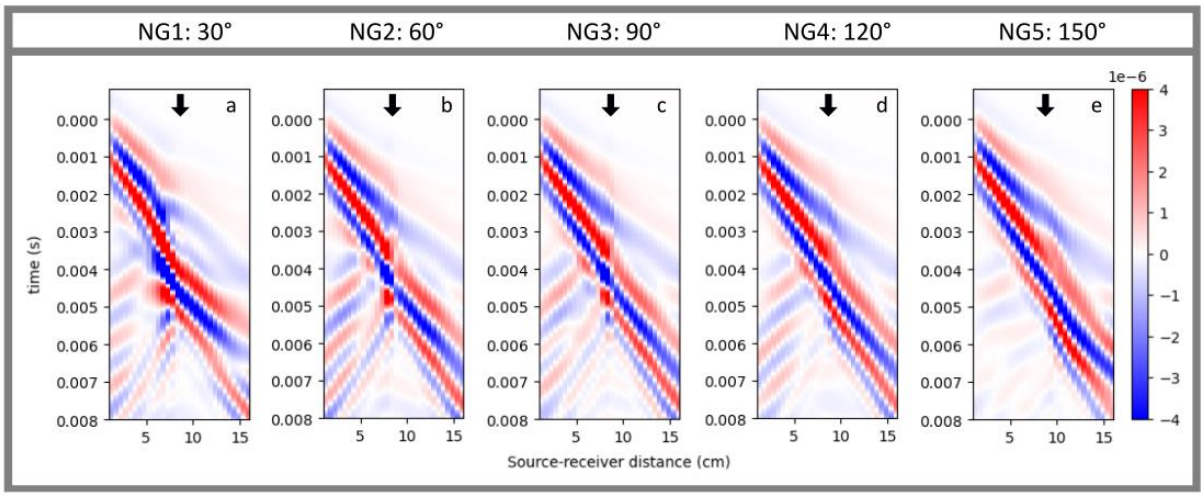

Figure 15: acoustic profiles of experiments NG1(a), NG2(b), NG3(c), NG4 (d) and NG5(e), with low density zone angle of 30° (a), 60°b), 90°(c), 120°(d) and 150° (d). The black arrow indicates the location of the low density zone.

4. Discussion

This section contains an interpretation of the influence of the studied deformation zone parameters on the wave behaviour in a granular medium. For that, a characterization of the limitations and uncertainties regarding the modelling methods is needed, as well as an interpretation of the general wave behaviour per modelling type. Thus, firstly an overview will be given for the physical modelling method in section 4.1, and for the numerical method in 4.2 before it is possible to discuss the results for the two parameter studies of fault properties in section 4.3 and fault geometry in 4.4.

4.1 Physical modelling and acoustics in granular media

4.1.1 Physical modelling method

The physical modelling results show that wave velocities contained some variation between the initial measurements of different models. This indicates there are still some unknown factors prior to the start of every experiment which are influencing the wave propagation. These factors could be environmental factors during sieving and measuring, the time between model preparation and measurements or the topography on the surface of the model.

Environmental factors during preparation and measuring of a model are a likely cause for the differences in signal to noise ratio, attenuation and variations in wave velocities (Smits et al., in prep.), which are all related to wave transmission through the medium. The most significant environmental factors that could have influenced the acoustic profiles in the experiments of this study are differences in temperature and humidity in the lab. It was observed that if temperature was fluctuating often or humidity remained high (60%-70%) over the course of the experiment, the signal to noise ratio of the data dropped significantly.

The time between model preparation and measurement was also observed to play an important role. If the model was prepared more than a couple hours before the actual experiment ran, then the wave transmission through the medium was significantly reduced, which is consistent with observations by Smits et al. (in prep.). This could again be caused by longer exposure to changing environmental factors.

Lastly it could also be possible that some of the surface topography that was created during the experiment had an impact on the surface waves in our experiment. The wire method used to create deformation zones also creates an elongated crater shape where the wire cut through the surface. Determining the impact of these surface structures is more difficult because they cannot be tested without the density anomaly. Thus it is possible that the acoustic refraction in the experiments using the wire technique is significantly altered by the surface topography and they are not fully representative for naturally generated fault structures with less surface topography, like strike-slip faults.

With these factors in mind, a couple measures can be taken to improve future experiments. For more consistent results with higher signal to noise ratio, better environmental control might be needed and time between preparation and measuring should be as short as possible. A smaller wavelength/higher frequency might be needed to properly image smaller structures at a higher resolution. With an improved set-up it could then also be possible to properly measure wave propagation in other granular materials which are less favourable for wave propagation than glass beads.

4.1.2 Laser vibrometry

Beside the previously discussed uncertainties within the experimental set up it is important to discuss effects related to the measuring methodology, which is still in development. Thus, a separate discussion on the important factors that impacted the model during experiments is useful for future use of this method.

Using a laser to generate waves is generally considered non-invasive, but unlike the CT scanner it does have some physical impact. The thermoacoustic effect of the laser slightly deforms the model when heating the surface, a small crater is formed at this location. These topographical changes might also have an impact on the acoustics of the model. However, the physical experiments do not show any impact from these surface structures on the acoustic waves, likely because they are too small scale to influence the wave propagation significantly. If a higher resolution would be tried in future experiments, this small scale topography could interfere with the imaging.

Increasing the resolution does have downsides however, the closer the resolution gets to the grainsize of the material the bigger the chance of scattering effects as well as increasing attenuation, thus lowering the signal to noise ratio (Krawczyk et al. 2013). It follows that smaller scale structures will generally be more difficult to image with a laser based set-up.

Lastly, in the current set up a multiple source single receiver system is used to make the acoustic profiles instead of a single source multiple receiver system. Generally, when studying wave propagation it is preferred to use a single source multiple receiver set up, because this allows to directly observe the behaviour of a single wave. However, the results of these two methods can be considered to be interchangeable based on the assumption that the source-receiver location does not matter because the travel time of a wave should be independent of wave propagation direction. This assumption holds for most cases, but becomes problematic when studying the effect of asymmetrical structures, in which case the wave propagation direction does matter. Hence when interpreting an asymmetrical structure with a multiple source single receiver set-up, this needs to be taken into account.

4.1.3 Wave behaviour

Every experiment resulted in similar wave features, besides slight differences in wave velocities. The most notable wave behaviour is the difference in the surface waves before and after shortening. After model preparation only 1 wave arrival can be observed, but after shortening of the model there are two distinguishable surface wave modes as seen in Figure 10d, e. Where the P-SV2 can be interpreted as the first mode of the surface wave, and the P-SV1 as the second mode of the surface wave. Where first mode travels the slowest because it has a shorter wavelength and therefore does not penetrate to the lower parts of the model with higher velocities (Zaccherini et al. 2021).

The different surface wave modes are however not always observed in physical modelling. Bodet et al. (2014) and Zaccherini et al. (2021) have both performed similar experiments, at 1500 and 500 Hz respectively, but instead of a laser to generate the waves they used a shaker. Bodet et al. observe only one P-SV mode, Zaccherini et al. (2021) however do observe the spilt of P-SV waves into two surface wave modes. An explanation for this difference is offered by the results of Zaccherini et al. (2021). They associate lower frequency signals (<600 Hz) with the two lowest order P-SV waves, and higher frequencies with more prominent P-waves. If the prominence of different wave types/modes is indeed dependent on the frequency of the source then this explains why Bodet et al. (2014), who used a higher frequency of 1500 Hz, did not observe the second mode.

This frequency dependency also highlights an important distinction between the shaker based experiments of these other studies and the laser based experiment done in this study. The former

experiments are more precise in the frequency range used in the experiments. Whereas the laser based experiments provide relatively little control because the thermoacoustic effect has a larger frequency domain (Scala & Doyle 1989). Because of this the laser based method generates more surface wave modes.

While in these examples there have not been more than two wave modes observed, Aleshin et al. (2007) had previously theorized an infinite number of possible surface wave modes in a granular medium based on an analytical solution of the Helmholtz equation. They also demonstrated that this multitude of modes transforms into a singular Rayleigh wave with increasing adhesion between grains, specifically they predict that in this transformation the first mode transforms into the Rayleigh wave and the other modes delocalize. This description is a good fit to the effect observed during shortening of the models in this study. The shortening of the model increases the stress, which would increase adhesion between grains. As a result, the P-SV2 wave, which is the first mode of the surface wave, increases in prominence as it starts to transform into the Rayleigh wave, and the other modes delocalize.

4.2 Numerical modelling and acoustics in granular media

The numerical model is a simplified version of the model used in the physical modelling. While it does generate waveforms with similar features to the Physical modelling, there are also still some interesting differences. It predicts some features, like boundary effects, that are not distinguishable in the physical modelling data and it fails to predict some features that are present in the physical modelling data.

In the numerical model set-up an expansion of the vertical dimension of the model was needed to fully remove the reflections of the bottom. These reflections were not strong, and also not distinguishable as bottom reflections. They did however significantly increase noise in the acoustic data. There was no reflection of the bottom observed in the physical experiments either, but taking into account that these reflections were significant in the numerical model it is possible that they were present in the physical model as well. They would not be distinguishable as bottom reflections, but they could have been increasing the noise level in the physical models. Thus, based on the numerical modelling, for further physical modelling a thicker model would be preferred, to eliminate the effect of bottom reflections.

The numerical model is not able to accurately predict all of the measurements from the physical model. The P-wave that is measured in the physical model travels significantly faster than the one in the numerical model. While the behaviour of the P-SV1 wave in the results is well predicted with the numerical model, the P-SV2 does not exist.

These differences could be caused by two factors, the resolution of the model, and the initial assumption the model operates on. The resolution of the numerical model is relatively low to keep computing time low. Thus it could be that the resolution was too low to predict some of the smaller scale features that do have a significant effect. Then the numerical model operates on the assumptions that the wave velocities can be properly predicted by equation 3 and that the stress field in the model is only dependent on the lithostatic stress. These two assumptions likely lead to a too simplified model that treats the material still like a fully adhesive block. According to Aleshin et al. (2007) different modes of the surface waves in a granular medium transform into a singular Rayleigh wave for increased adhesion. Thus, this could be the reason the model only simulates the first mode of the surface wave,

Despite these differences in features of the acoustic waves in the numerical and physical models, the numerical modelling should still give reliable predictions on the behaviour of the P-wave and the first

mode of the surface wave when interacting with the deformation zone. But, to better predict the wave behaviour in future experiments, the resolutions of the model could be increased further and the stress field could be better defined to see what the effect would be of an added horizontal stress component.

4.3 Fault Properties

There are two fault properties studied with two different modelling methods. The thickness of the deformation zone was studied using physical modelling. The density contrast of deformation zones was studied using numerical modelling. Both experiments were performed to determine whether it is possible to image the shear zones created by faulting. Firstly a discussion will be had on the effects per parameter, followed by what these results mean for the imaging of faults in physical modelling.

The results obtained in experiment PP1-PP4 (see Figure 11) show the impact of the deformation zone thickness. The placement of the deformation zone can already be observed in the models where they have a thickness of 3 mm or higher. The acoustic profiles show a lesser wave amplitude at the location of the deformation zone, but there is no lasting effect on the wave. The models with deformation zones of >4 mm do however have a lasting effect on the wave. For those models the P-SV wave partly reflects, which becomes more prominent with increasing thickness of the low density zone.

The thicknesses of some of the artificially made deformation zones are similar to the actual faults. The thrust faults in the numerical modelling were measured to have a thickness of about 3-4 mm while the grain size due to sieving was 0.3 mm or less. This coincides with earlier observations by Pouliquen and Gutfraind (1996), who found that the thickness of the shear zones scales with the particle size, being approximately equal to 10-15 particle diameters. Thus, the fish wire-created deformation zones are most comparable to the thrust faults, while the metal wire and rope create an exaggerated deformation zone thickness. The results of this experiment indicate that a regular thrust fault should at least show up in an acoustic profile as an area of decreased wave amplitude. But the thickness of faults in this medium are not large enough to reflect a observable amount of the wave with this set-up. The connection between grain size and deformation zone thickness could indicate that deformation zones in granular materials with larger grain sizes could be easier to image, because these thicker deformation zones are more likely to produce reflections.

The numerical modelling results of experiment NP1-NP4 (see Figure 14), which shows the effect of different density contrasts, indicate that both the P-wave as well as the P-SV wave will reflect of off a lower density zones. However the conditions at which they do are different. At a density contrast of 13% only the P-wave reflects. However, for density contrasts of 35% and higher both the P-wave and the P-SV wave reflect. The amount of density decrease in deformation zones in physical models is about 9–16%. Thus the numerical modelling results suggest that natural faults have a strong enough density difference to reflect the P-waves but not to reflect the P-SV wave.

This reflection of P-waves in the numerical modelling is not a feature that is observed in the physical modelling results. Thus it is unlikely the current set-up used can effectively image P-wave reflections. It could however indicate that more precise measurements could also show P-wave reflections. This would then allow for imaging of faults.

4.4 Fault geometry

The physical and numerical modelling experiments investigating wave characteristics on the geometry of the deformation zones were run with nearly identical model set-ups. This allowed the resulting datasets to be easily compared. Firstly the interpretation method for the physical results

will be discussed, followed by the results per modelling method, and finally a general interpretation of the impact of deformation zone dip direction and dip angle on acoustic waves.

To discuss the physical modelling results it is necessary to address the fact that these experiments contain asymmetrical fault structures in the cross-sectional view. Such structures, as discussed earlier, are problematic for the direct interpretation of the wave behaviour because of the single receiver multiple source set-up used in this study, which result in the waves of different sources approaching the fault structure from different sides. As such, the deformation zone either dips towards or away from the wave propagation direction depending on where the source is located within a single acoustic profile.

To account for this effect, the acoustic profiles can be segmented into two parts depending on which side of the deformation zone the source is located. Then, to complete the profile from the point of view of the wave, one side of an acoustic profile can be combined with the other side of a different profile where the dip direction is mirrored. In this way both sides of experiment PG1 can combined with the corresponding other side of PG5 and vice versa for PG2 and PG4, experiment PA3 does not have this issue because the structure is symmetrical. The following observations are made with this method.

The results of experiments PA1-PA5 show a clear correlation between the geometry of the deformation zone and the wave behaviour. The most significant factor of the geometry is the dip direction. When a surface wave hits a deformation zone that dips away from it, it passes through the deformation zone without reflecting, see PG5 and PG1 in Figure 12f, j. When a surface wave hits a deformation zone that dips towards it, then it does not pass through and partly reflects back. Buddensiek (2009) has done a similar experiment with a deformation zone that dipped against the wave propagation direction, which also showed clear reflections. The effect of the deformation zone appears similar for the dip angles of 30 and 60 degrees. For the vertical deformation zone a combination of both the features described for the two dip directions can be observed. The P-SV wave travels partly through the deformation zone, while also partly reflecting. Thus the dip direction clearly has a large influence on wave behaviour, but the influence of the dip angle cannot clearly be seen, with the used set-up.

In the numerical experiments NG1-NG5 a similar effect can be observed regarding the interaction between the P-SV wave and deformation zones geometry. When an acoustic wave hits a deformation zone that dips way from it, it passes through the deformation zone without reflecting, see NG5 and NG1 inFigure 15a, e. When a surface wave hits a deformation zone that dips towards it, then the P-SV does pass through but also partly reflects. Similar to the other numerical model results, P-wave reflections can also be seen. These reflection get less when the angle increases from 30 to 150 degrees, but do always appear. It is possible that the same is true for the P-SV wave, but that signal strength for those waves reduces faster with increasing dip angle.

The fact that the same behaviour is obtained in the numerical data as in the physical data shows that this wave behaviour can be explained using the assumption made for the numerical modelling. Thus, the dependency of the acoustic wave velocity on bulk density and depth can be used to explain this behaviour.

5. Conclusion

Deformation zones within a granular medium create distinctive acoustic wave profiles. The deformation zone properties like deformation zone thickness, deformation zone geometry(fault dip angle) and the density contrast between the deformation zone and bulk material were found to have a strong effect.

The thickness of the deformation zone affects the reflection coefficient of the acoustic surface waves, where the thicker the zone is the more of the wave reflects. This makes it more favourable to image thicker deformation zones. The density contrast also affects the reflection coefficient, the larger the density difference between the deformation and the surrounding material is, the more of the wave reflects.

Based on the effect of these two tested deformation zone properties, the laser vibrometry method is more reliable when imaging exaggerated deformation zones. For actual fault in the granular medium the reflections of the P-SV wave might not be observable, because these fault zones are too thin and have not enough density contrast. However, the numerical models imply that these reflections still occur but at a lower signal strength, which could not be distinguished with the current set-up. this method could be improved by reducing the signal to noise ratio. It might be possible to observe surface wave reflection at these lower properties, or even observe P-wave reflections. If those could be observed, it would be possible to map fault structures using the laser vibrometry method.

Based on both the numerical and physical modelling results the geometry of a deformation zone also significantly affects acoustic waves. If the deformation zone dips away from the wave propagation direction, the surface wave has a very low reflection coefficient and passes through the zone relatively unaltered. When the deformation zone dips towards the source the reflection rate is high and little of the wave passes through the deformation zone, it partly reflects back. This effect is most clearly dependent on dip direction, but lesser differences can also be observed based on the dip angle of the deformation zone. The congruent results from the physical modelling and numerical modelling strongly support this dependency of the reflection of surface waves on dip direction of a deformation zone.

However, in all experiments ran in this study, the most significant results were obtained for reflections of surface waves, and none for body waves. This means that with the current set-up it is possible to image certain surface structures. To properly image internal faults in a granular medium, measurements with a higher signal to noise ratio are needed to better study the behaviour of the other waveforms. Currently, the only information on the internal structure can be obtained indirectly by using the deformation zone geometry dependence of the acoustic waves to infer the continuation of a fault.

6. Bibliography

Adam, J., Urai, J. L., Wieneke, B., Oncken, O., Pfeiffer, K., Kukowski, N., ... & Schmatz, J. (2005). Shear localisation and strain distribution during tectonic faulting—New insights from granular-flow experiments and high-resolution optical image correlation techniques. *Journal of Structural Geology*, *27*(2), 283-301.

Afanasiev, Michael and Boehm, Christian and van Driel, Martin and Krischer, Lion and Rietmann, Max and May, Dave A and Knepley, Matthew G and Fichtner, Andreas., 2019, Modular and flexible spectral-element waveform modelling in two and three dimension, Geophysical Journal International, 10.1093/gji/ggy469

Aleshin, V., Gusev, V. and Tournat, V., 2007. Acoustic modes propagating along the free surface of granular media. *The Journal of the Acoustical Society of America*, *121*(5), pp.2600-2611.

Bergamo, P. and Socco, L.V., 2016. P-and S-wave velocity models of shallow dry sand formations from surface wave multimodal inversionVP and VS model of dry sand with SW. *Geophysics*, *81*(4), pp.R197-R209.

Bodet, L., Jacob, X., Tournat, V., Mourgues, R. Gusev, V., 2010, Elasticity profile of an unconsolidated granular medium inferred from guided waves: Toward acoustic monitoring of analogue models, Tectonophysics 496 99–104

Bodet, L., Dhemaied, A., Martin, R., Mourgues, R., Rejiba, F., & Tournat, V., 2014, Small-scale physical modeling of seismic-wave propagation using unconsolidated granular media. *Geophysics*, *79*(6), T323-T339.

Buddensiek, M.L., 2009, Seismic Imaging of Sandbox Models, Dissertation

Colletta, B., J. Letouzey, R. Pinedo, J. F. Ballard, and P. Bale, 1991, Computerized X-ray tomography analysis of sandbox models: examples of thin skinned thrust systems: Geology, 19, 1063–1067. Purnell, 1986

Chen, K., Fu, X., Dorantes-Gonzalez, D. J., Li, Y., Wu, S., & Hu, X. (2013). Laser-Generated Surface Acoustic Wave Technique for Crack Monitoring-A Review. *Int. J. Autom. Technol.*, *7*(2), 211-220.

Dewhurst, R. J., Hutchins, D. A., Palmer, S. B., & Scruby, C. B. (1982). Quantitative measurements of laser-generated acoustic waveforms. *Journal of Applied Physics*, *53*(6), 4064-4071.

Gassmann, F. 1951. Elastic waves through a packing of spheres. *Geophysics*, *16*(4), 673-685.

Hubbert, M. K. (1937). Theory of scale models as applied to the study of geologic structures. *Bulletin of the geological society of America*, *48*(10), 1459-1520.

Jacob, X., Aleshin, V., Tournat, V., Leclaire, P., Lauriks, W. and Gusev, V.E., 2008. Acoustic probing of the jamming transition in an unconsolidated granular medium. *Physical Review Letters*, *100*(15), p.158003.

Klinkmüller, M., Schreurs, G., Rosenau, M. and Kemnitz, H., 2016. Properties of granular analogue model materials: A community wide survey. *Tectonophysics*, *684*, pp.23-38.

Koyi, H. (1997). Analogue modelling: from a qualitative to a quantitative technique—a historical outline. *Journal of Petroleum Geology*, *20*(2), 223-238.

Krawczyk, C.M., Buddensiek, M.L., Oncken, O. and Kukowski, N., 2013. Seismic imaging of sandbox experiments–laboratory hardware setup and first reflection seismic sections. *Solid Earth*, *4*(1), pp.93-104.

Liu, C.H. and Nagel, S.R., 1992. Sound in sand. *Physical review letters*, *68*(15), p.2301.

Mandl, G., De Jong, L. N. J., & Maltha, A. (1977). Shear zones in granular material: an experimental study of their structure and mechanical genesis. *Rock mechanics*, *9*, 95-144.

Nam, B. H., Kim, J., An, J., & Kim, B. (2013). A review on the effects of earthborne vibrations and the mitigation measures. *International Journal of Railway*, *6*(3), 95-106.

Panien, M., Schreurs, G., Pfiffner, A.O., 2006. Mechanical behaviour of granular materials, used in analogue modelling: insights from grain characterisation, ring-shear tests and analogue experiments. Journal of Structural Geology 28 (9), 1710–1724

Pouliquen, O. and Gutfraind, R., 1996. Stress fluctuations and shear zones in quasistatic granular chute flows. *Physical Review E*, *53*(1), p.552.

Purnell, G. W., 1986, Observations of wave velocity and attenuation in two-phase media., *Geophysics*, *51*(12), 2193-2199.

Scala, C. M., & Doyle, P. A. (1989). Time-and frequency-domain characteristics of laser-generated ultrasonic surface waves. *The Journal of the Acoustical Society of America*, *85*(4), 1569-1576.

Schmid, T. C., Schreurs, G., & Adam, J. (2022). Characteristics of continental rifting in rotational systems: New findings from spatiotemporal high resolution quantified crustal scale analogue models. *Tectonophysics*, *822*, 229174.

Sherlock, D. H., 1999, Seismic imaging of sandbox models: PhD thesis, Curtin University of Technology.

Smits, J., Beekman, W.W.W., Willingshofer, E., Vasconcelos, I., in prep. Laser based monitoring of granular material experiments.

Tournat, V. and Gusev, V. E., 2010. Acoustics of unconsolidated “model” granular media: An overview of recent results and several open problems. *Acta Acustica united with Acustica*, *96*(2), 208-224.

Wegner, S., Stannarius, R., Boese, A., Rose, G., Szabo, B., Somfai, E. and Börzsönyi, T., 2014. Effects of grain shape on packing and dilatancy of sheared granular materials. *Soft Matter*, *10*(28), pp.5157-5167.

Zaccherini, R., Palermo, A., Marzani, A., Colombi, A., Dertimanis, V.K. and Chatzi, E.N., 2021. Attenuation of surface modes in granular media. *arXiv preprint arXiv:2111.07199*.

Zwaan, F., Schreurs, G., & Adam, J. (2018). Effects of sedimentation on rift segment evolution and rift interaction in orthogonal and oblique extensional settings: Insights from analogue models analysed with 4D X-ray computed tomography and digital volume correlation techniques. *Global and planetary change*, *171*, 110-133.

Zwaan, F., & Schreurs, G. (2023). A novel method for analogue modelling of lithospheric-scale rifting, monitored through X-Ray CT-scanning, at the University of Bern Tectonic Modelling Laboratory (Swit.

APPENDIX I

Signal to noise ratio of Quartz sand versus Glass beads

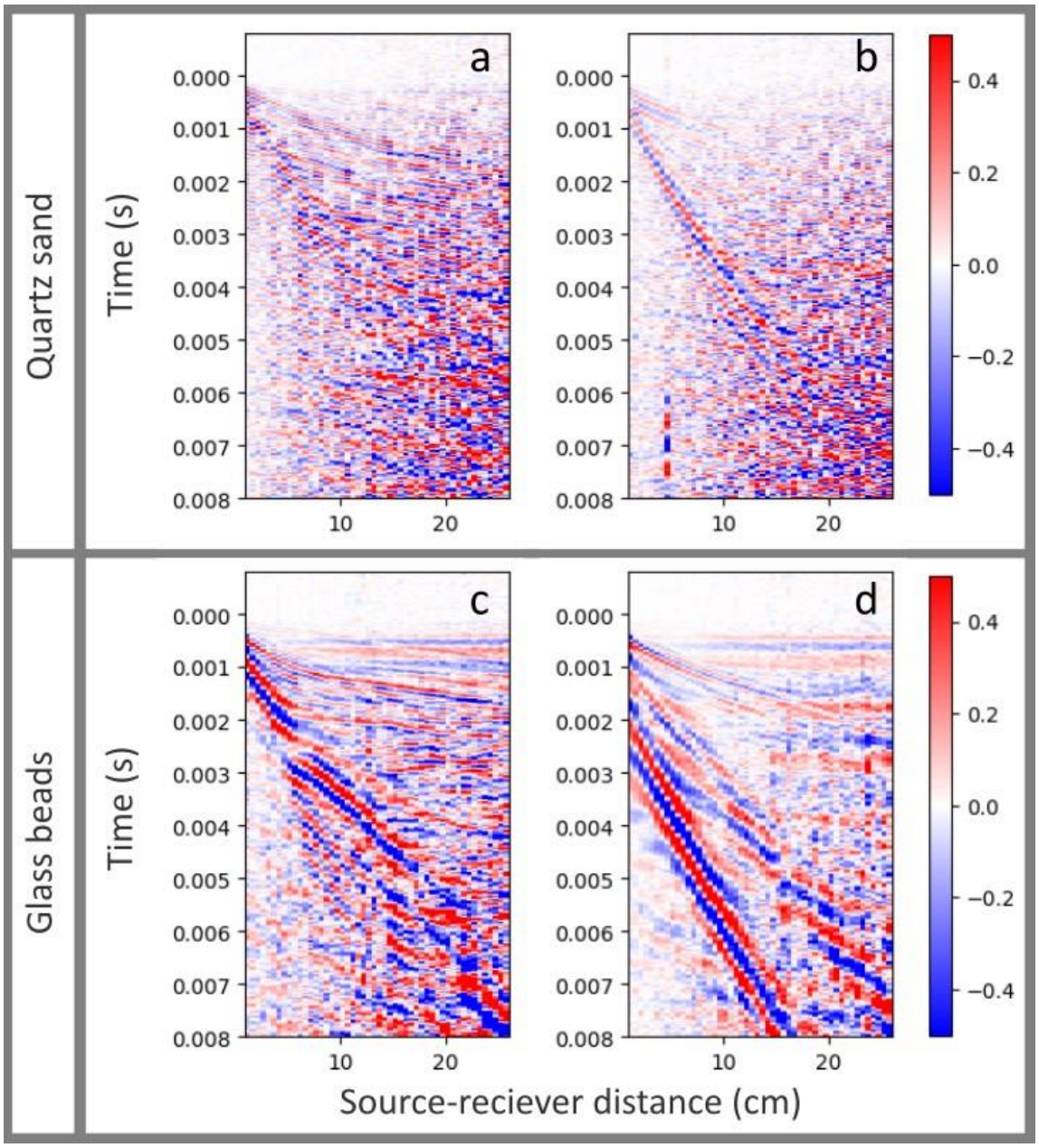

Figure I: Comparison between results in quartz sand versus glass beads. Acoustic profiles for Quartz sand(a,b) and Glass beads(c,d) in the same experimental set-up. For a nondeformed model(a,c) and after shortening has been applied(b,d).